# Electrochemical Characterization of Evolving Ionomer/Electrocatalyst Interactions Throughout Accelerated Stress Tests

Leiming Hu[1], Tim Van Cleve[1], Haoran Yu[2], Jae Hyung Park[3], Nancy Kariuki[3], A. Jeremy Kropf[3], Rangachary Mukundan[4ǂ], David A. Cullen[2], Deborah J. Myers[3], KC Neyerlin[1*]

1. Chemistry and Nanoscience Center, National Renewable Energy Laboratory, Golden, CO, USA
2. Center for Nanophase Materials Sciences, Oak Ridge National Laboratory, Oak Ridge, TN, USA
3. Chemical Sciences and Engineering Division, Argonne National Laboratory, Lemont, IL, USA
4. Materials Physics and Applications Division, Los Alamos National Laboratory, Los Alamos, NM, USA

ǂ Current Address: Energy Technologies Area, Lawrence Berkeley National Laboratory, Berkeley, CA 94720

*Corresponding author: Kenneth.Neyerlin@nrel.gov

There has been an increased interest in utilizing polymer electrolyte membrane fuel cells (PEMFCs) for heavy-duty vehicle (HDV) applications, necessitating a thorough understanding of electrocatalyst degradation mechanisms as well as the evolution of electrode structures and interactions that determine end-of-life performance. To examine the degradation of PEMFC catalyst layers used for HDV, a catalyst-specific accelerated stress test (AST) was applied to various membrane electrode assemblies (MEAs) for 90,000 cycles. The degradation of high surface area carbon supported dispersed Pt (Pt/HSC), annealed Pt (a-Pt/HSC) and PtCo (PtCo/HSC) alloy catalysts were examined by measuring the change of mass activity, $O_2$ transport resistance, electrochemical active surface area (ECSA), catalyst accessibility and ionomer-electrocatalyst interactions. Compared to a-Pt/HSC and Pt/HSC catalyst, the PtCo/HSC showed better initial mass activity and a larger initial mass transport loss. It also experienced faster degradation after the first 30k AST cycles, as a large portion of Co leached out during potential cycling. As for Pt/HSC, while it showed higher initial performance relative to a-Pt/HSC, it also suffered from faster degradation. STEM characterizations show that the ECSA losses are largely related to Pt dissolution resulting in either catalyst particle growth via the Ostwald ripening mechanism or redeposition in the membrane. Catalyst accessibility measured by CO stripping showed decreased RH sensitivity of catalyst accessibility for all three samples, which could be related to dissolved Pt predominantly redeposited on the exterior of the carbon support at the end of test or carbon support structure change due to carbon corrosion. Further characterization utilizing CO displacement revealed lower sulfonate adsorption at the end of test indicating Pt redeposition occurred preferentially near ionomer hydrophobic domains. CO impedance measurements showed that the water-covered Pt and carbon surfaces are decreasing relative to the ionomer covered Pt and carbon surface, which may be related to structural changes in the carbon support (e.g. from carbon corrosion), or alterations in ionomer morphology within the catalyst layer.

## Introduction

Recently released United States Department of Energy (DOE) fuel cell targets puts an emphasis on longer lifetimes and higher fuel efficiency for heavy-duty vehicle (HDV) applications.[1,2] In the U.S., medium and heavy duty vehicles are responsible for around 25% of the transportation greenhouse gas emissions.[3] Compared to PEMFC powered light-duty vehicle (LDV), HDV have more predictable routes, which could accelerate commercial adoption with much lower infrastructure investment. However, HDV also require a much longer lifetime and mileage than LDV. The U.S. DOE durability target for HDV is 30,000 hrs, equivalent to vehicle lifetime range of 1 million miles.[2] Hence, improving the PEMFC system durability, especially the catalyst layer durability during extended operation becomes important for maintaining system efficiency, reducing fuel cost and enabling lower total cost of ownership.

The state-of-the-art PEMFC catalyst layer (CL) contains carbon supported Pt or PtCo alloy catalyst bound together by Nafion ionomer, which facilitates proton transport.[4] The morphology and distribution of the catalyst nanoparticles, the catalyst/ionomer interactions and the structure of the carbon support are critical to the CL's performance and durability.[5,6] For Pt nanoparticles, the degradation mainly comes in two ways, Pt mass loss and particle coarsening.[7,8] It has been shown that Pt solubility will increase with electrode potential until around 1.1 V, and then decreases at higher potentials due to oxide layer formation.[9,10] The dissolved Pt can migrate to the cathode/membrane interface and then get reduced by hydrogen to form Pt crystals i.e., "Pt band", in the membrane phase.[11,12] Alternatively, Pt ion can redeposit to nearby nanoparticles, leading to particle growth (i.e., Ostwald ripening). It has also been reported that nearby Pt nanoparticles can migrate and coalesce into larger particles. In terms of PtCo alloy catalyst, a higher oxygen reduction reaction (ORR) activity can be achieved compared with Pt catalyst due to sub-surface Co element strain effect.[13] During long-term operations, however, Co can also dissolve into acidic polymer electrolyte at electrode potentials higher than 0.1 V.[14,15] Unlike dissolved $Pt^{2+}$ ion, which can redeposit at low electrode potentials, dissolved $Co^{2+}$ can hardly be reduced, because the $Co/Co^{2+}$ has a lower redox potential than $H_2/H^+$ in acidic environment.[13,16] During voltage cycling, transition metal will slowly leach out leading to decrease of intrinsic activity of PtCo alloy catalyst.[17] The increased concentration of $Co^{2+}$ in the ionomer phase leads to increased oxygen transport resistance and decreased high-current-density performance.[18] Papadias *et al.*[19] investigated PtCo catalyst with different Co content and initial morphology, and found that the voltage losses induced by AST are related to increased kinetic and mass transfer losses, with a combined effect of Co leaching and ECSA loss. Carbon support is another factor that can affect the catalyst durability. Compared with low surface area carbon support, high surface area carbon (HSC) can provide better initial dispersions for Pt, and catalyst nanoparticles located inside the carbon support tends to have better initial activity as it is free from sulfonate group poisoning effect.[20,21] It has been reported that catalyst nanoparticles on HSC have reduced coalescence.[7,22] However, HSC supported catalyst can still undergo severe electrochemical active surface area (ECSA) loss due to Pt dissolution and Ostwald ripening.[22] O'Brien *et al.*[23] conducted durability study of PtCo catalyst on different porous and solid carbon supports, and found that porous carbon supports can slow down the catalyst particle dissolution/precipitation, but also exhibit greater transport resistance due to enhanced Co leaching.

The aim of this study is to examine the durability of several HSC supported Pt (dispersed - Pt/HSC, annealed - a-Pt/HSC, and alloyed PtCo - PtCo/HSC) catalysts and elucidate the changes in catalyst properties and catalyst-ionomer interactions induced from long-term operation. Membrane electrode assemblies (MEAs) containing these catalysts were exposed to 90k cycle catalyst-specific accelerated stress tests (ASTs) with periodic electrochemical diagnostics applied to examine the changes in catalyst activity, accessibility, ionomer coverage, sulfonate interaction, and electrochemical surface area. Improving the understanding the state of the electrode structure at the end of test informs both material design directions (e.g. catalyst design and support morphology), as well as engineering opportunities (e.g. higher loadings and novel structures) that can subsequently improve efficiency and reduce total cost of ownership for heavy duty vehicles.

## Experimental

***Membrane Electrode Assembly***. – Three types of cathode catalyst with 50 wt.% metal loading were used for this study, i.e., HSC supported dispersed Pt catalyst (Pt/HSC, TEC10E50E, TANAKA precious metals, Japan), annealed Pt catalyst (a-Pt/HSC, ElystPt500550, Umicore, Germany), and PtCo catalyst (PtCo/HSC, ElystPt500690, Umicore, Germany). Catalyst coated membranes (CCMs) were fabricated with an anode loading of 0.05 $mg_{Pt}/cm^2$ (Pt/HSC, ElystPt200390, Umicore, Germany) and a cathode loading of 0.25 $mg_{Pt}/cm^2$ with an ionomer (Nafion D2020 dispersion, Fuel Cell Store) to carbon ratio (I:C ratio) of 0.83. For Umicore a-Pt/HSC and PtCo/HSC catalyst, Nafion HP membrane was used. For Pt/HSC catalyst, Nafion 211 membrane was used. The membrane electrode assembly was assembled by sandwiching the CCM between two 50 cm$^2$ Freudenberg H23C8 (Fuel Cell Store, USA) gas diffusion layers (GDLs). The gasket is polytetrafluoroethylene (PTFE) film with a chosen thickness to achieve a GDL compression ratio of ca. 18%.

***MEA Testing Protocols***. – The MEAs were tested using a 14-channel serpentine flow field, as was used in previous study by Baker *et al.*[24]. For integral cell test, CCMs with 50 cm$^2$ active surface were used. For differential cell test, the CCM active surface area was masked down to 5 cm$^2$ using PTFE gasket. The cells were installed with a bolts' torque of 40 in-pounds. For 5 cm$^2$ differential cell test, the assembled cell was installed in a co-flow configuration, and for 50 cm$^2$ integral cell testing, a counter-flow configuration was used.

Break-In Procedures. During the break-in procedure, the cell temperature was maintained at 80 $^{o}$C, with anode hydrogen flow rate of 1.5 slpm and cathode air flow rate of 3.7 slpm. The break-in was done by holding the cell voltage at 0.6 V and 0.9 V with each potential hold of 4 mins and cycled for a total break-in time of 4 hours.

Voltage Recovery. The voltage recovery (VR) was done by maintaining the cell temperature at 40 $^{o}$C and running the cell voltage of 0.1 V for 2 hrs. During this period, the anode $H_2$ flow rate was 0.1 slpm and the cathode air flow rate was 0.5 slpm. The VR helps improve electrochemical performance of the cell across the entire fuel cell potential range, as has been previously reported.[25]

Polarization Curves. $H_2/O_2$ polarization curves were obtained at 80$^{o}$C cell temperature, 100% RH and 100 kPa $O_2$ partial pressure (150 kPa absolute cell pressure). Current density value was recorded at each cell voltage for 4 mins and in an anodic direction, starting from low cell voltage of 0.75 V up to open circuit voltage (OCV). $H_2$/air Polarization Curves were obtained at different cell temperatures and RH conditions using constant current mode (2.25 – 0.01 A/cm$^2$). The stochiometric ratio was 1.5 at the anode and 2 at the cathode.

Oxygen Limiting Current Measurement. Oxygen limiting current measurements were conducted on differential cells and at 80$^{o}$C, 75/30% RH. Three different oxygen concentrations (2%, 3% and 5%), and four different total gas pressures (100, 150, 200 and

300kPa) were used. At cell voltage of 0.3, 0.24, 0.18, 0.12 and 0.06 V, limiting current was recorded for 3 mins, with the maximum current densities at cell voltage above 0.12 V was taken as the actual limiting current. More information regarding oxygen limiting current measurement can be found in previous work by Baker *et. al*. [24]

CO Stripping Voltammetry. CO stripping voltammetry was tested at 30%, 50%, 75% and 100% RH to obtain the ECSA. During the measurement, the cell temperature is 80$^{o}$C. The cathode was fed with CO at a gas flow rate of 0.25 slpm for two mins followed by a $N_2$ purge at the same flow rate for another two mins. Then at $H_2$/$N_2$ environment, the cyclic voltammetry (CV) was performed at a potential range from 0.05 V to 0.9 V, with a scan rate of 20 mV/s. The CO stripping charge was obtained from the first anodic sweep. 420 $\mu C/cm^2$ was used as the area specific charge to convert the stripping charge to ECSA.

CO Displacement Chronoamperometry. This test was done by measuring the transient current response at a constant electrode potential caused by introducing CO.[26,27] During the measurement, Pt surface adsorbed cationic/anionic species will be displaced by CO and result in a displacement charge ($q_{dis}$). The CO displacement measurement was done at 0.1, 0.2, 0.3 and 0.4 V and at 30%, 50%, 75% and 100% RH conditions.

Capacitance Coverage Measurement. The test was conducted by measuring electrochemical impedance spectroscopy (EIS) at $H_2$/$N_2$ environment and $H_2$/CO environment (Gamry Reference 3000, Gamry Instruments).[28] During the measurement, the cell is at 80$^{o}$C and 1 atm backpressure. 1% CO/$N_2$ gas mixture was supplied to the cathode at 1 slpm. The EIS was measured from 20kHz to 0.1 Hz with a sine wave magnitude of ±1.5 mV. The cathode potential was hold at 0.45 and 0.2 V versues reversible hydrogen reference electrode (RHE) for CO-free and CO-doped experiment, respectively. More information regarding this method can be found in previous work by Van Cleve *et al*.[28]

Accelerated Stress Test. The standard catalyst durability AST was used following the U.S. Hydrogen and Fuel Cell Technologies Office multi-year research, development, and demonstration (MYRD&D) plan protocol [29]. The fuel cell MEAs were cycled between 0.6 V and 0.95 V, with a holding time of 2.5 s at each potential and a ramping time is 0.5

s with a ramping rate of 700 mV/s. The AST voltage profile is shown in the inset of Figure 1b. During the AST cycles, the cell was operating at 80°C in $H_2/N_2$ environment and 100% RH.

***Electron Microscopy Characterizations***. In preparation for diamond knife ultramicrotomy, a-Pt/HSC, PtCo/HSC and Pt/HSC MEAs at BOT, 30k, and 90k were embedded in epoxy. Cross sections of each MEA were cut to a thickness between 50 and 75 nm. Scanning transmission electron microscopy (STEM) and energy-dispersive X-ray spectroscopy (EDS) measurements were performed using a Talos F200X transmission electron microscope (Thermo Fisher Scientific) operated at 200kV and equipped with Super-X EDS system with 4 SDD windowless detectors. Particle size distributions consisting of ~1000 were obtained from high-angle annular dark-field (HAADF) images (0.1 nm pixel resolution, 200 nm by 200 nm field of view) using a custom Python code.[30] The Co composition for each MEA was obtained from EDS elemental maps of the full electrode (21 nm pixel resolution, 10.9 μm field of view) which was processed with Esprit 1.9 Software (Bruker).

***Small and Wide-Angle X-ray Scattering Characterization.***

X-ray scattering data acquired at beam line 9-ID-C at the Advanced Photon Source (APS) were utilized to determine the catalyst particle size and lattice spacings of the PtCo particles in the cathode catalyst layers of the beginning of test, 30K AST-cycled, and 90K AST-cycled MEAs. The cathode catalyst layers were transferred from the membrane to Scotch brand Magic tape (3M) using a press and peel method. Monochromatic 21 keV X-rays were focused to a beam spot size of 0.8 × 0.2 mm. The scattered X-ray intensity was obtained over a range of scattering angles/scatterer dimensions using the combined ultra-small-angle X-ray scattering (USAXS), pinhole small-angle X-ray scattering (pinSAXS), and wide-angle X-ray scattering (WAXS) using the combination of a Bonse-Hart camera for USAXS and a Pilatus 100 K detector for pinhole SAXS and WAXS.[31,32] The complete scattered intensity, I(q), was then obtained by combining the USAXS ($10^{-4}$ to

$6\times10^{-2}$ Å$^{-1}$) and the pinhole SAXS ($3\times10^{-2}$ to 1 Å$^{-1}$). The WAXS data covered a d-spacing range from approximately 6 Å to 0.8 Å. The background scattering from a piece of Scotch brand Magic was subtracted from the scattering data for each sample.

The SAXS data were background corrected and reduced with the NIKA software package,80 and data analysis was conducted using the IRENA software package.81 Both packages were run on IGOR Pro 7.0 (Wavemetrics). Particle size distributions were obtained from the measured scattering data using the maximum entropy (MaxEnt) method, which involves a constrained optimization of parameters to solve the scattering equation:

$$I(q) = |\Delta\varrho|2 \int |\mathrm{F}(\mathrm{q},\mathrm{r})|2 \left(\mathrm{V}\ (\mathrm{r})\right)2\ \mathrm{Np}\ (\mathrm{r})\mathrm{dr}_{int} \qquad [1]$$

where I(q) is the scattered intensity, $\varrho$ is the scattering length density of the particle, and F(q,r) is the scattering function at scattering vector q of a particle of characteristic dimension r. V is the volume of the particle, and Np is the number density of particles in the scattering volume.

The WAXS data analysis utilized powder diffraction multi peak fitting 2.0, an Irena macro.[33] The position of the (311) scattering peak was utilized to determine the lattice spacing and this spacing was then utilized to calculate the Pt to Co ratio in the crystalline portions of the catalyst particles using Vegard's law and the nearest neighbor (NN) distances of 2.7747 Å and 2.4917 Å for Pt and Co, respectively, as determined from fitting the extended X-ray absorption spectroscopy data for Pt and Co foils, respectively, as shown in Myers *et al.*[34] and Vegard's law.

### *X-ray Absorption Fine Structure Spectroscopy Characterization.*

X-ray absorption spectroscopy (XAS) was used to determine the atomic structure of the PtCo catalyst in the cathode catalyst layers of the beginning of test, 30K AST-cycled, and 90K AST-cycled MEAs. X-ray spectra were acquired at the Pt $L_3$ edge in the fluorescence geometry at beamline 10-ID at the Advanced Photon Source (APS) at Argonne National Laboratory. The second derivative of the X-ray absorption near edge spectrum (XANES) of Pt foil, located downstream of the samples, was used to calibrate the Pt $L_3$-edge energy to 11567 eV. At least three spectra were acquired for each sample and merged (averaged) using the merge function of the Athena software.[35] Spectra were processed and the data analyzed using the Athena/Artemis/ifeffit codes. The data are presented as the magnitudes and the real parts of the Fourier transforms of the extended regions of the spectra from k values of 3 to 14.5 keV.

## Results and discussion

$H_2/O_2$ polarization curves for Pt/HSC, a-Pt/HSC and PtCo/HSC MEAs are shown in Figure 1a. The beginning of test (BOT) performance of the PtCo/HSC sample has better oxygen reduction reaction (ORR) kinetics compared with the a-Pt/HSC sample, with about 30 mV higher cell voltage at 100 mA/cm$^2$. The mass activity based on iR-free current density at 0.9 V is shown in Figure 1b. The PtCo/HSC has about two times higher BOT mass activity compared with a-Pt/HSC sample. After the first 30k AST cycles, the PtCo/HSC sample shows a significant cell voltage loss, and the mass activity dropped by 71.3% from 877 mA/mg$_{Pt}$ to 252 mA/mg$_{Pt}$. It is known that the high mass activity of the PtCo alloy catalyst largely comes from the geometric strain created by Co element.[36] The rapid decrease during the first 30k AST cycles suggests a large portion of Co leached out from the alloy, which is supported by the WAXS and STEM-EDS characterizations and will be discussed in a later section. From 30k to 90k AST cycles, PtCo/HSC and a-Pt/HSC samples show similar degradation rates, as the mass activity values continued to decrease by 12.3% and 19.6%, respectively. The Pt/HSC catalyst also shows higher initial mass activity compared with a-Pt/HSC but with a faster degradation rate. After 90k AST cycles, the mass activity of Pt/HSC dropped by 83% with an end of test (EOT) mass activity lower than a-Pt/HSC.

Figure 2 shows $H_2$/air polarization curves at BOT and after 90k AST cycles. At low-current-density regions, the PtCo/HSC has about 35 mV higher cell voltage compared with Pt catalyst at 80°C, 100% RH condition, and 16 mV higher at 90°C, 65% RH. However, PtCo/HSC MEA also shows higher BOT losses at high-current-density regions, which has been reported to be associated with $Co^{2+}$ leaching during the sample fabrication process and the conditioning process.[34] After 90k AST cycles, the cell voltage difference between PtCo/HSC and a-Pt/HSC at low-current-density region becomes less significant, the PtCo/HSC sample also shows larger high-current-density voltage loss compared with a-Pt/HSC. After AST cycles, a-Pt/HSC sample shows a relatively stable high-frequency resistance (HFR). In contrast, there is a slight increase in HFR for PtCo/HSC sample. The larger high-current density losses track with increased HFR values for PtCo/HSC sample, which again suggests $Co^{2+}$ migration into the ionomer phase both in the catalyst layer and in the membrane. After 90k cycles, the Pt/HSC based MEA exhibited the largest performance degradation among these three samples.

.

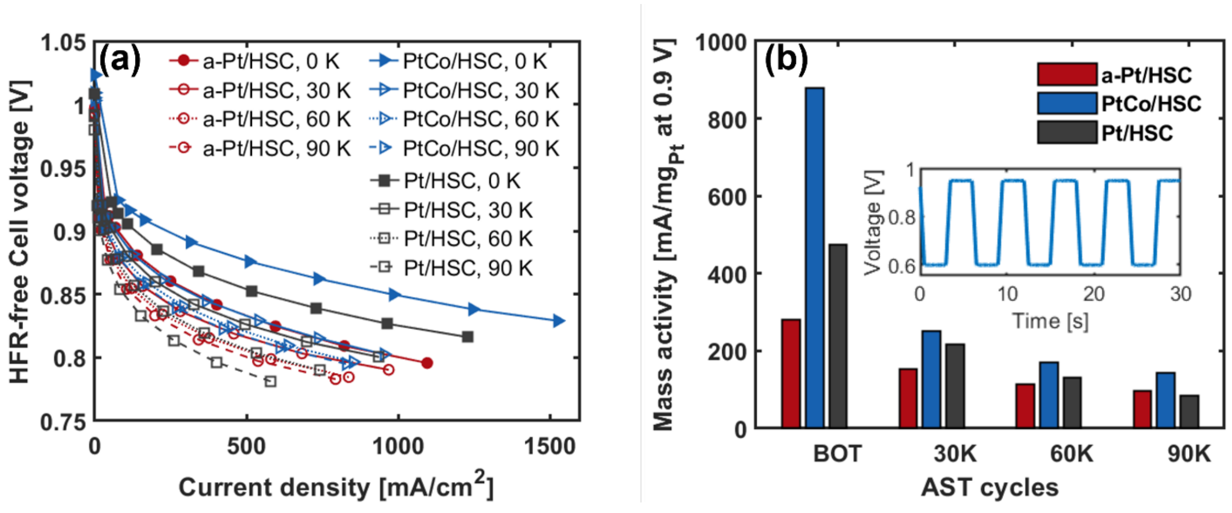

Figure 1. (a) $H_2$/$O_2$ polization curves of Pt/HSC, a-Pt/HSC and PtCo/HSC samples (b) Mass activity of Pt/HSC, a-Pt/HSC and PtCo/HSC samples measured at BOT and after 30K, 60K and 90K AST cycles. Measurements were conducted with 50 $cm^2$ integral cell at 80°C, 100% RH and 150kPa absolute pressure.

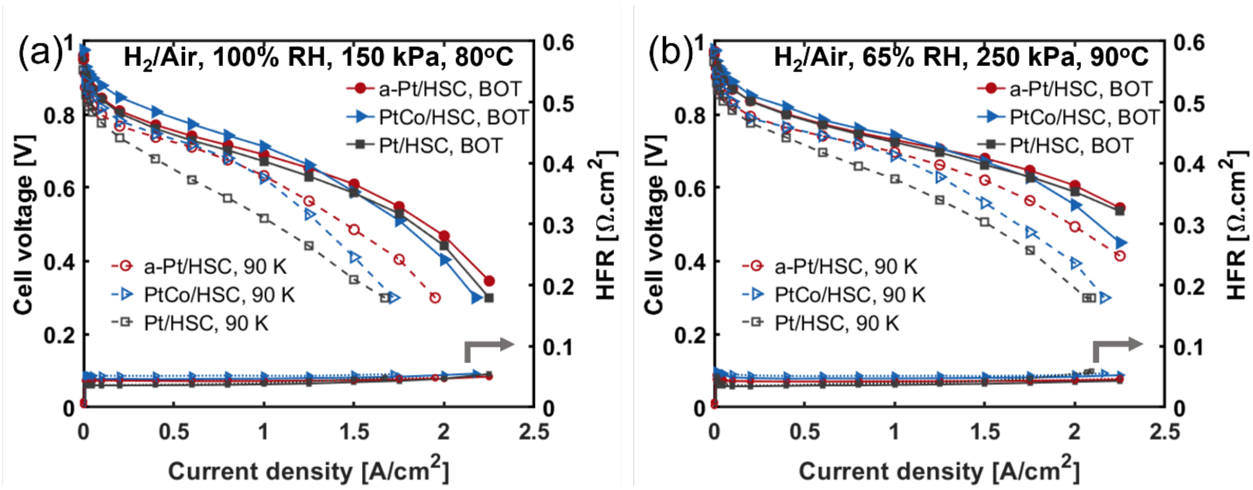

Figure 2. BOT (solid lines) and after 90k AST cycles EOT (dashed lines) air polarization curves of Pt/HSC, a-Pt/HSC and PtCo/HSC MEAs measured at (a) 80°C, 100% RH and (b) 90°C, 65% RH. Measurements were conducted with 50 cm$^2$ integral cell

CV curves were measured for Pt/HSC, a-Pt/HSC and PtCo/HSC MEAs at different stages of the durability test. As shown in Figure 3, the PtCo/HSC sample BOT CV curve shows a broad featureless H-adsorption/desorption peak, which can be related to the Co alloying effect,[17] while in contrast, both Pt/HSC and a-Pt/HSC samples show distinct characteristic peaks correspond to different facets of Pt nanoparticles at 0.05 – 0.4 V potential range. After 30k AST cycles, similar characteristic peaks start to show on PtCo/HSC sample, suggesting a leaching out of Co element from the alloy catalyst and less alloying effect. This loss of Co alloying effect is also evident from WAXS measurement results as shown in Figure S1. For a-Pt/HSC sample, scattering peaks corresponding to different Pt facets get sharper after AST cycles. However, the peak location remains the same. In contrast, the peaks for PtCo/HSC sample have slightly different locations compared to a-Pt/HSC sample and keep shifting towards Pt-related locations. The Fourier transform of the X-ray absorption spectroscopy data acquired at the Pt $L_3$ edge also supports the WAXS data showing loss of Co from the Pt lattice after AST cycling. As shown in Figure S4, the Pt-Pt scattering in the 2.4 to 3 Angstrom region shifts towards larger radial distances with AST cycling, approaching the Pt-Pt scattering path length of the Pt foil reference (Figure S4). Figure 3b presents the ECSA at different stages of AST cycles measured using CO stripping. During the first 30k AST cycles, all three samples exhibit a more pronounced ECSA loss. The a-Pt/HSC sample shows a 41% ECSA loss (40 to 23 $m^2_{pt}/g_{pt}$), and the PtCo/HSC sample shows 31% ECSA loss (34 to 23 $m^2_{pt}/g_{pt}$) after the first 30K AST cycles. The Pt/HSC sample has the largest extent of ECSA loss, down by 56% (62 to 27 $m^2_{pt}/g_{pt}$) after the first 30K AST cycles. From 30k-90K cycles, the a-Pt/HSC and PtCo/HSC samples show similar ECSA loss, while the Pt/HSC shows a faster ECSA loss, likely due to its substantially smaller initial particle size of 2.2 nm. It should be noted that the ECSA here is normalized based on the BOT Pt loading. As shown in the Figure S5, after 90K AST cycles, Pt gets redeposited to the membrane and form Pt-band. For a-Pt/HSC, around 33.0% of Pt from the cathode catalyst layer gets redeposited to the membrane after 90K AST cycles. The ratio of Pt loss to the membrane is 36.3% for PtCo/HSC sample and 27.4% for Pt/HSC sample. Through the entire 90K cycles, the a-Pt/HSC and PtCo/HSC show similar ECSA retention, with a ECSA loss of 61% (or 42% after correction by taking into consideration of Pt loss to the membrane) and 54% (28% after correction), respectively. In contrast, the Pt/HSC has a total ECSA loss of 77% (68% after correction).

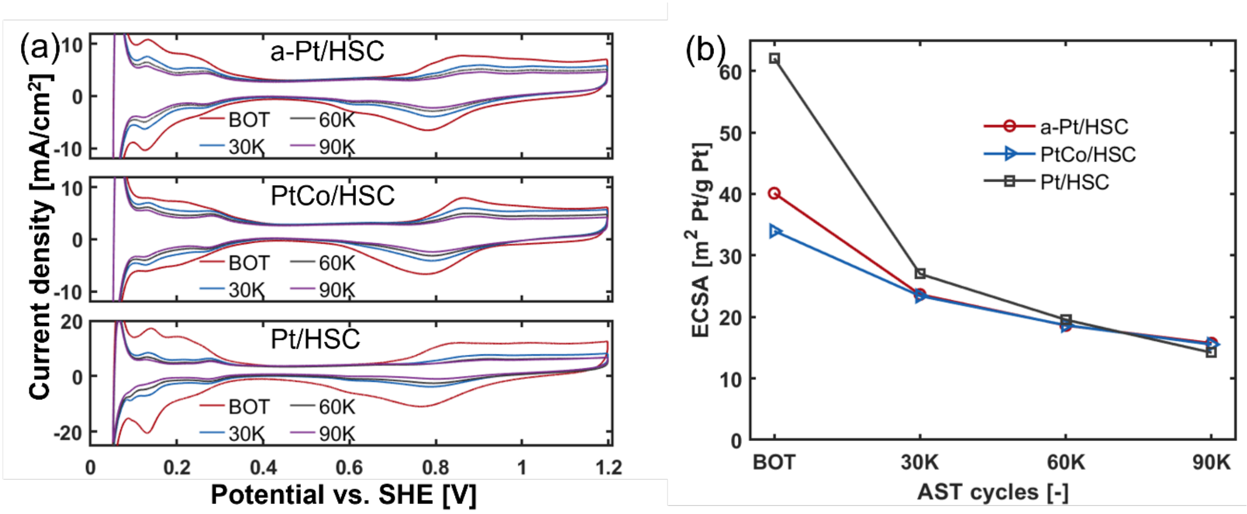

Figure 3. (a) Cathode CV of Pt/HSC, a-Pt/HSC and PtCo/HSC sample measured at 30$^o$C and 95% RH. (b) The change of ECSA versus number of AST cycles obtained from CO stripping measurement.

The catalyst accessibility was measured via CO stripping voltammetry at different RH conditions. At low RH conditions, only the Pt surface that is in direct contact with Nafion ionomer can be accessed through CO stripping, while at high RH, Pt inside the carbon pores can also be active during CO stripping measurement.[37] The change of ECSA of Pt at different RH conditions provides information about the relative amount of Pt located inside carbon pores and at the exterior of the carbon support, or Pt surface in catalyst aggregates/agglomerates that has not been covered by ionomer. Figure 4 shows plots of normalized ECSA as a function of RH and cycle number to aid in the visualization of catalyst accessibility. Both the a-Pt/HSC and PtCo/HSC sample had a BOT catalyst accessibility of ~70%, while the Pt/HSC sample had a BOT catalyst accessibility of 45% at 30% RH. As the AST cycling continued, even though the overall ECSA values for all three samples decreased, the Pt accessibility continually increased. After 90k AST cycles, the catalyst accessibility for a-Pt/HSC and PtCo/HSC increased to 95% and 93% respectively, when 30% RH was used as the lower bound. This change in catalyst accessibility caused by catalyst durability AST cycles corresponds well with previous studies by Ramaswamy *et al.*[17] There are several possible factors that may cause this catalyst accessibility change. During the AST cycles, a large portion of Pt or PtCo catalyst located inside the carbon support could coalesce to larger particles, leading to loss of ECSA for catalyst located inside carbon support. The Pt of internal catalyst may dissolve and preferentially redeposit to the outside of the carbon support. During the AST, there is inevitably small amounts of carbon corrosion, which could open up internal pores and lead to increased Pt accessibility.

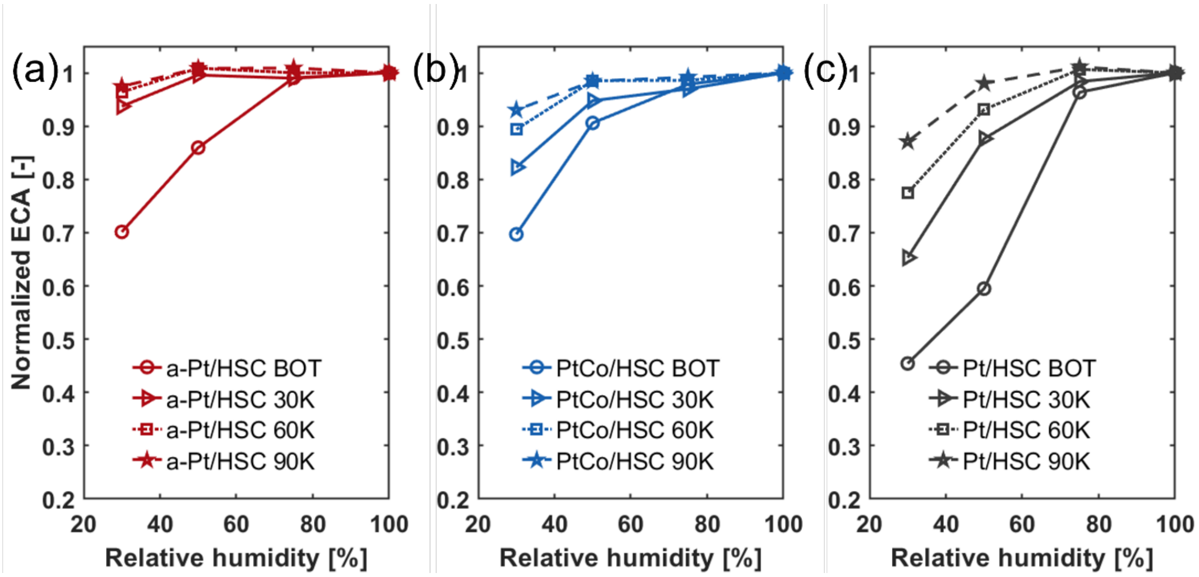

Figure 4. ECSA of (a) a-Pt/HSC, (b) PtCo/HSC and (c) Pt/HSC samples measured by CO stripping voltammetry method at different RH conditions and at BOT, after 30k, 60k and 90k AST cycles.

To examine changes in catalyst morphology during AST cycles, STEM images were taken from three types of MEAs. Figure 5a-i, b-i and c-i show the particle size distributions (PSD) of these three MEA samples at BOT, after 30K and after 90K AST cycles. Figure 5a-ii, b-ii and c-ii are the corresponding representative HAADF images. The PSD results show an increase of average particle size for all three samples. In this study, the median particle size increased from 2.2 to 4.8 nm, from 4.4 to 5.9 nm, and from 4.5 to 6.3 nm for the Pt/HSC, a-Pt/HSC, and PtCo/HSC samples respectively after 90k cycles. Mean particle diameter data for a-Pt/HSC, and PtCo/HSC samples are shown in the Table S1 and agrees well with the particle size measured by STEM approach. From STEM-EDS analysis, the PtCo/HSC has a BOT Co content of 24 at.%. The Co atomic content dropped to 18 at.% after the first 30K AST cycles and then further decreased to 13 at.% after 90K AST cycles. By comparison, fitting of the wide angle X-ray scattering (WAXS) data showed Co contents in the PtCo crystallites of 26, 15, and 10 at.% at BOT and after 30K and 90K AST cycles, respectively, as listed in Table S1. The difference between the TEM-EDS and WAXS data can be attributed to TEM-EDS detecting Co in the ionomer phase of the electrode as well as Co in the PtCo crystallites. It should be noted that the Pt/HSC PSD at

EOT has a distinct bimodal distribution, with a group of particles remained at an average particle size similar to BOT stage, and another group of particles with significantly increased particle size. This unique bimodal distribution might be related to the stability difference of internal and external Pt particles. However, it may require electron tomography characterizations and is beyond the scope of this study.

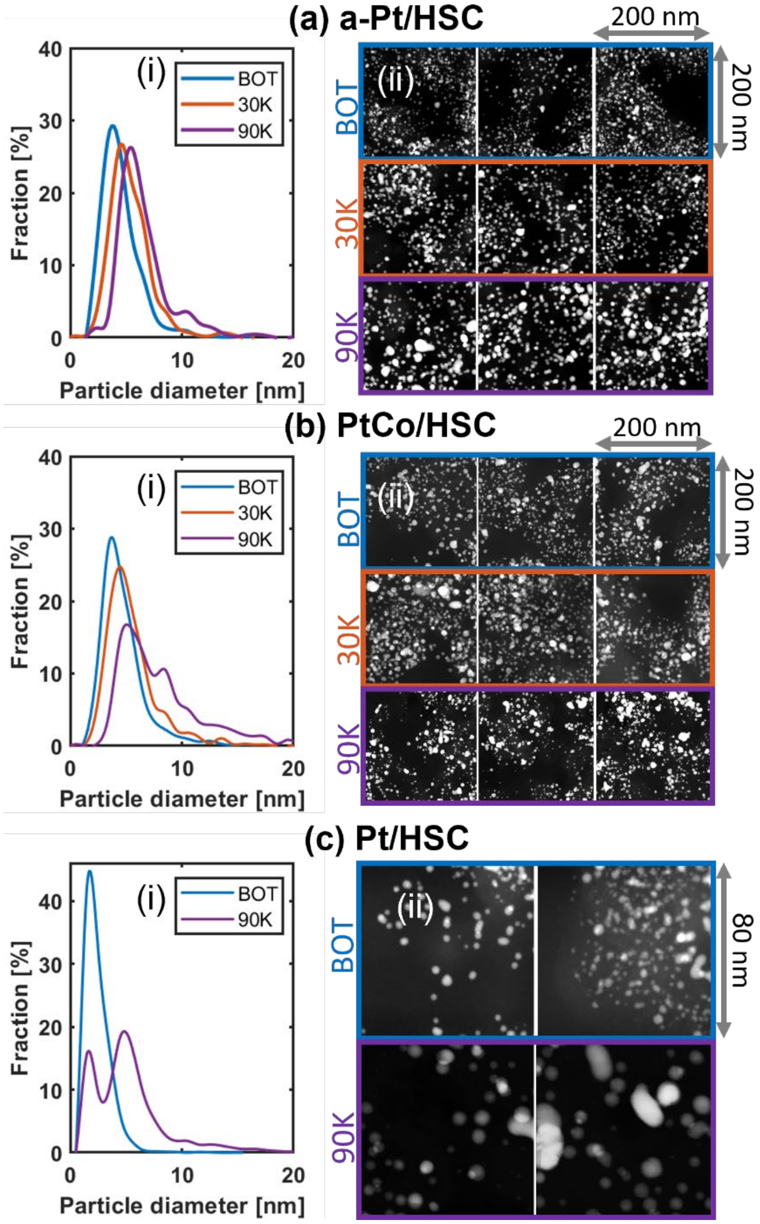

Figure 5. Particle size distribution and corresponding STEM images of a-Pt/HSC (a-i,ii), PtCo/HSC (b-i,ii) and Pt/HSC (c-i,ii) cathode obtained at BOT, 30K and 90K AST

cycles. Measurements were conducted on a separate set of 5 $cm^2$ samples that went through the same amount of catalyst specific AST cycles

To better understand the high-current-density voltage losses and help elucidate the impact of change in catalyst accessibility, catalyst particle growth, and loss of catalyst to the membrane, $O_2$ limiting current measurement were conducted at different stages of AST cycles. The non-Fickian $O_2$ transport resistance ($R_{NF}$) values are shown in Figure 6. At BOT, the $R_{NF}$ of PtCo/HSC sample is about 110% higher compared to a-Pt/HSC sample. The high initial $R_{NF}$ can explain the higher BOT mass transport loss for PtCo/HSC sample, as shown in Figure 2, and is related to the initial $Co^{2+}$ leaching during the sample preparation process and the conditioning process.[34] The BOT $R_{NF}$ value for a-Pt/HSC and Pt/HSC correspond well with the empirical equation presented in previous work by Kongkanand *et al.*[38], which correlates Pt roughness factor with the catalyst layer $R_{NF}$. This makes sense since all the materials examined in that study were at BOT. After AST cycles, however, the $R_{NF}$ value for a-Pt/HSC and Pt/HSC start to deviate from the empirical equation. In addition to Pt redistribution, increasing $R_{NF}$ can be attributed to structural and interfacial modifications in the electrode, potentially resulting from carbon corrosion or alterations in ionomer/catalyst interactions.

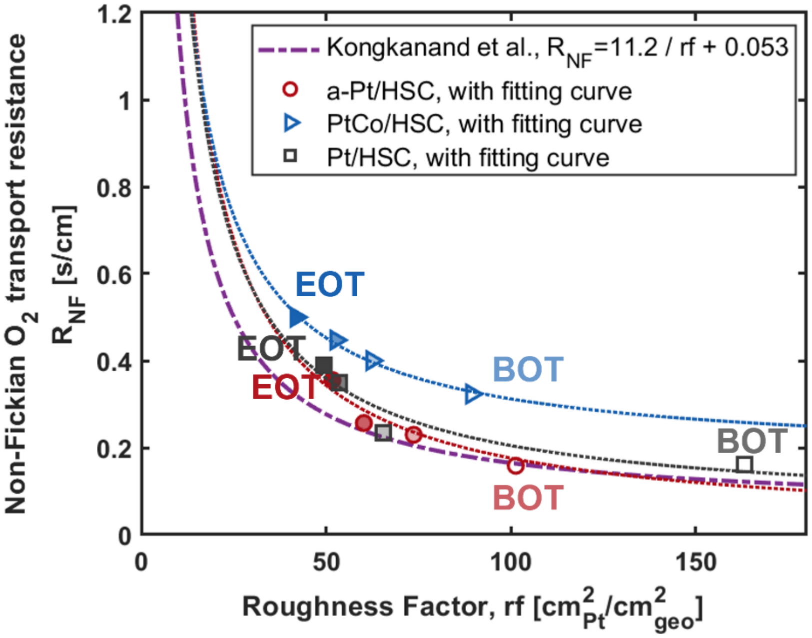

Figure 6. Non-Fickian $O_2$ transport resistance of Pt/HSC, a-Pt/HSC and PtCo/HSC sample at BOT and after certain AST cycles conducted on 5 $cm^2$ differential MEAs. The empirical equation is from Kongkanand *et al.* [38]

While accessibility measurements can relay a global depiction of Pt accessibility, to yield a more intimate examination of each electrodes evolving electrochemical interfaces, the relative change of Nafion ionomer coverages on both the carbon support and Pt electrocatalyst were examined using $H_2/N_2$ impedance. Here, the double layer capacitance was used to separate ionomer and water coverage and Pt and carbon surfaces by measuring capacitance at both low (20%) and (100%) RH conditions, with and without CO introduced to the cathode.[28] Shown in Figure 7, as the AST proceeds, the double layer capacitance representing water coverage on Pt surface for all three types of MEAs keeps decreasing, suggesting a reduction in accessibility of Pt located inside the carbon support. As the Pt/water ($Pt_{water}$) interactions decreased, the signal from carbon/water ($C_{water}$) interfaces also decreased. This can indicate either the collapse of internal carbon structure resulting from localized carbon corrosion, which has a reversible potential of 0.207 V [39] and is enhanced by Pt decorating the support, or the presence of more hydrophobic carbon pores due to the movement of Pt from the pore to the carbon support surface. Though it has been shown that the relative Pt surface in direct contact with ionomer increased with AST cycles (see Figure 4), utilizing the capacitive approach we can also glean that the Pt/ionomer interactions overall either increased, as is the case for the a-Pt/HSC, or stayed relatively constant, as was the case for both PtCo/HSC and Pt/HSC.

Probing deeper, the capacitive approach also illustrates enhancements in carbon/ionomer ($C_{ionomer}$) interactions across all three electrodes as a function of AST cycle. When coupled with reduced carbon/water interactions and the fact that the overall carbon capacitance does not significantly change for any of the three electrodes, the data could indicate an increased pore width and/or a cycling induced mobilization of the ionomer into carbon mesopores over the test duration. In recent work, Kikkawa and Jinnouchi [40] used molecular dynamics simulations to illustrate the impact of solvent composition on ionomer penetration into mesopores >2 nm. They concluded that alcohol rich inks suppressed ionomer penetration, while pure water inks promoted penetration. In this work, alcohol rich inks were used, which would explain the relatively higher Pt/water and C/water interactions at BOL. However, few studies have examined the effect of potential and electrochemical conditioning on ionomer conformation and coverage. Previously, Paul and Karan demonstrated that exposure to high temperature annealing resulted in reduced conductivity for ionomer thin films, while subsequent exposure to liquid water enabled higher conductivity across a range of RH [41]. Additionally, Neyerlin and coworkers [25] previously illustrated that MEA break-in procedures had a more pronounced effect on non-Fickian resistances for internally accessible electrocatalysts (i.e. those supported on porous carbons) when compared to externally accessible electrocatalysts (e.g. Pt/Vu), pointing to the importance of understanding operando morphology versus as-prepared MEAs. This study builds on our previous one, where now one can clearly observe that carbon/ionomer interactions are influenced by electrochemical potential, with the bulk of those changes occurring in the first 30k cycles for all three materials. In fact, the majority of changes for all interfaces occur within the first 30k cycles, with only Pt/ionomer interactions remaining stable from BOT to 30k for the PtCo/C and Pt/C electrodes. In contrast, Pt/ionomer interactions increase significantly within the first 30k cycles for the a-Pt/C electrode. Nevertheless, what remains unclear is the extent to which purportedly detrimental Pt/sulfonate interactions are affected, further hindering interfacial transport resistances[28] and/or electrochemical kinetics.

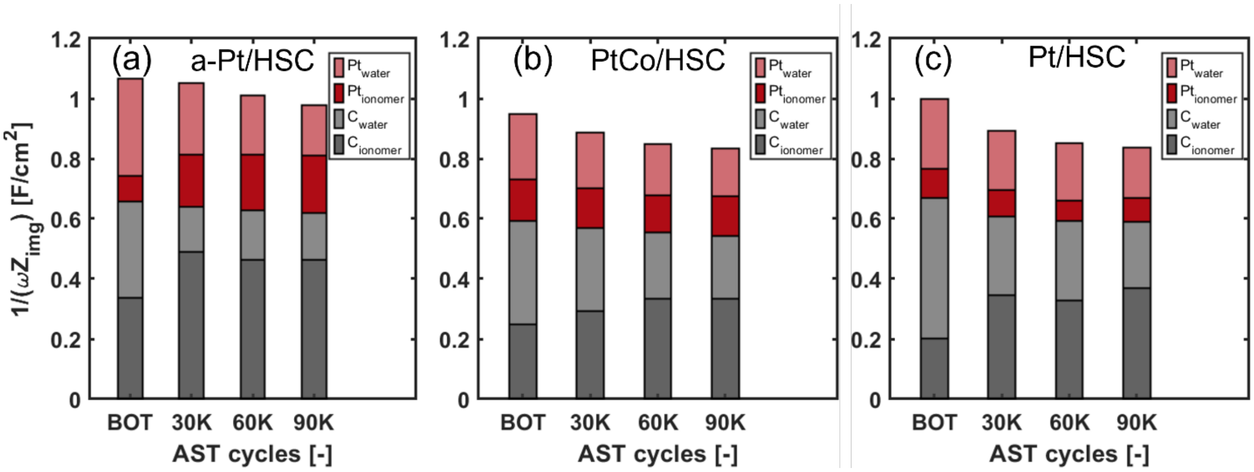

Figure 7. Double layer capacitance contributions from Pt/ionomer ($Pt_{ionomer}$), Pt/water ($Pt_{water}$) and carbon/ionomer ($C_{ionomer}$) and carbon/water ($C_{water}$ interfaces obtained from impedance measurement of the (a) Pt and (b) PtCo samples at BOT and after AST cycles.

Understanding the interfaces at EOT will enable a more prescribed design for both material and engineering approaches to optimize the efficiency of heavy-duty fuel cells. To further probe the change of ionomer/catalyst interactions during durability test, CO displacement measurements were conducted. Different from CO stripping method, which probes all electrochemically active Pt surface, the CO displacement charge is proportional to the amount of Pt surface that is in direct interaction with sulfonate sidechains from Nafion ionomer.[26,27] Differences in CO stripping, CO displacement, and CO impedance method are illustrated in Figure 9b. CO displacement method has been previously used by Garrick *et al.*[26] and Van Cleve *et al.* [27,28] to study the ionomer/catalyst interaction on different catalyst layers. Perego *et al.* [42] recently used this method to study the changes in ionomer/catalyst interaction under AST cycles. They found that under catalyst AST, the catalyst layer sulfonate coverage is decreasing at both humidified and dry conditions and attributed the coverage change to the chemical degradation of ionomer. The sulfonate coverage presented in Figure S3 is the CO displacement charge normalized by the CO stripping charge from the corresponding ECSA measurement at that RH condition. Because the BOT ECSA has a strong RH dependence, the calculated BOT sulfonate coverage of all three MEAs show higher values at dryer conditions. Different from Perego *et al*.'s work,[42] the sulfonate coverage of the three MEA samples at 100% RH remain relatively the same or slowly increase with AST cycles. The difference in the trend of sulfonate coverage change vs. AST cycles at 100% RH is probably related to different type of catalyst used in this study. Similar to Perego *et al*.'s work,[42] we see that the sulfonate coverage at dry conditions decreases with AST cycles. Figure 8 shows the dry sulfonate coverage calculated as the ratio of sulfonate displacement charge relative to the Pt surface in direct contact with the ionomer measured at 30% RH. The decrease of sulfonate coverage in dry condition is more likely related to Pt preferentially deposited at the hydrophobic domain of the catalyst/ionomer interface during AST cycles, as the ionomer coverage on carbon. Pt based on CO impedance measurement as shown in Figure 7 suggests no significant ionomer degradation.

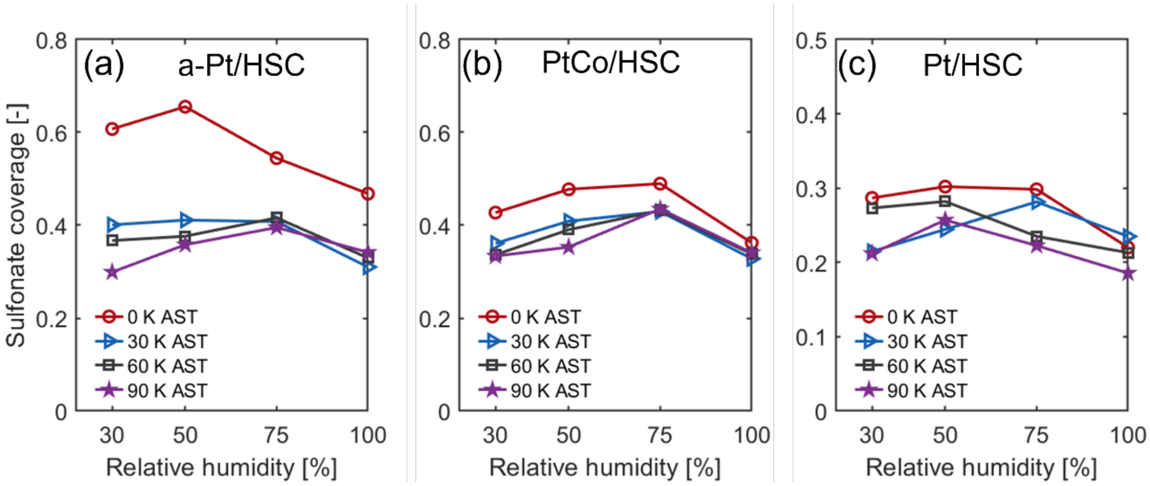

Figure 8. Sulfonate coverage using CO displacement charge measured at 0.4 V at different RHs and normalized by ECSA value from dry condition for (a) a-Pt/HSC, (b) PtCo/HSC and (c) Pt/HSC MEA samples at BOT, after 30k, 60k and 90k AST cycles.

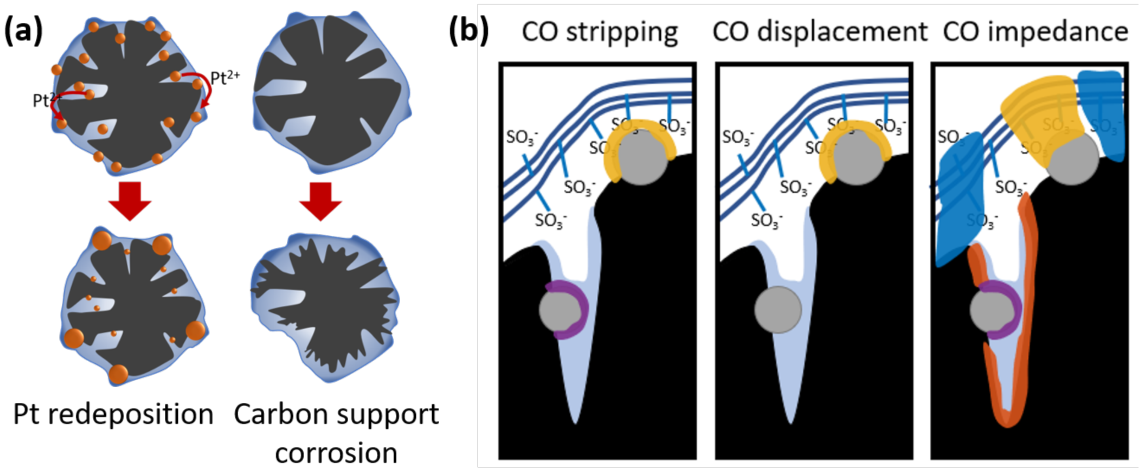

Figure 9. (a) Illustration of possible degradation mechanisms induced by AST cycles. (b) Illustration of different regions probed by CO stripping, CO displacement and CO impedance method.

## Conclusions

This work investigated the degradation of fuel cell catalyst layer for heavy-duty vehicle applications. MEAs with three different types of cathode catalyst, Pt/HSC, a-Pt/HSC and PtCo/HSC, were studied under 90K catalyst specific AST cycles. The PtCo/HSC sample showed much higher BOT mass activity compared to the a-Pt/HSC sample. The mass activity enhancement becomes less significant beyond 30K cycles due to leaching of Co from the catalyst particles, decreasing the intra-particle strain induced by alloying, as supported by the WAXS and STEM-EDS analysis. The Pt/HSC also showed higher initial mass activity but also suffers from faster degradation due to catalyst dissolution and redeposition. From the ECSA measurement, the a-Pt/HSC and PtCo/HSC sample show similar trend of ECSA loss from 30K to 90K AST cycles, while the well dispersed Pt/HSC suffered from more significant ECSA loss. From the $H_2$/air polarization curves, the PtCo/HSC sample has a higher BOT mass transport resistance compared with a- Pt/HSC and Pt/HSC sample. The PtCo/HSC sample's mass transport loss becomes more significant after AST cycles. The catalyst accessibility measurement at different RH conditions using CO stripping method revealed that all three catalysts show less RH sensitivity after AST cycles, which may be a combination of Pt preferentially redepositing on the exterior of the carbon support and carbon support corrosion leading to a change in pore structure and hydrophobicity, as illustrated in Figure 9a. CO impedance measurement suggest that there is an increase in the exterior ionomer thickness, probably due to shrinking of the overall carbon support size caused by slow carbon corrosion, or dielectric constant change due to ionomer re-orientation. The sulfonate coverage study indicates that Pt preferentially redeposits to the hydrophobic domains at the ionomer/catalyst interface.

## Acknowledgement

This work was authored in part by Alliance for Sustainable Energy, LLC, the manager and operator of the National Renewable Energy Laboratory for the U.S. Department of Energy (DOE) under Contract No. DE-AC36-08GO28308. This material is based on work performed by the Million Mile Fuel Cell Truck ($M^2FCT$) Consortium, technology manager Greg Kleen. Funding was provided by the U.S. Department of Energy, Office of Energy Efficiency and Renewable Energy, Hydrogen and Fuel Cell Technologies Office (HFTO). The X-ray scattering experiments were performed at beamline 9-ID-C at the Advanced Photon Source (APS) at Argonne National Laboratory (ANL). The X-ray spectroscopy experiments were performed at beamline 10-ID at the APS, which is operated by the Materials Research Collaborative Access Team (MRCAT). Use of the APS, an Office of Science user facility operated by ANL, is supported by the U.S. Department of Energy, Office of Science, Office of Basic Energy Sciences, under Contract No. DE-AS02-06CH11357. MRCAT is supported by DOE and by the MRCAT member institutions. The Talos F200X S/TEM tool was provided by US DOE, Office of Nuclear Energy, Fuel Cycle R&D Program, and the Nuclear Science User Facilities. RM acknowledges the support of Los Alamos National Laboratory under Contract No, 89233218CNA000001 operated by

Triad National Security, LLC. The views expressed in the article do not necessarily represent the views of the DOE or the U.S. Government. The U.S. Government retains and the publisher, by accepting the article for publication, acknowledges that the U.S. Government retains a nonexclusive, paid-up, irrevocable, worldwide license to publish or reproduce the published form of this work, or allow others to do so, for U.S. Government purposes.

## References

[1] D.A. Cullen, K.C. Neyerlin, R.K. Ahluwalia, R. Mukundan, K.L. More, R.L. Borup, A.Z. Weber, D.J. Myers, A. Kusoglu, New roads and challenges for fuel cells in heavy-duty transportation, Nat. Energy. (2021) 1–13.

[2] J. Marcinkoski, R. Vijayagopal, E. Adams, B. James, J. Kopasz, R. Ahluwalia, Hydrogen Class 8 Long Haul Truck Targets (US Department of Energy, 2019, n.d. https://www.hydrogen.energy.gov/pdfs/19006_hydrogen_class8_long_haul_truck_targets.pdf.

[3] B.P. Center, Annual Energy Outlook 2020, Energy Inf. Adm. Washington, DC. (2020).

[4] V. Yarlagadda, M.K. Carpenter, T.E. Moylan, R.S. Kukreja, R. Koestner, W. Gu, L. Thompson, A. Kongkanand, Boosting fuel cell performance with accessible carbon mesopores, ACS Energy Lett. 3 (2018) 618–621.

[5] R.L. Borup, A. Kusoglu, K.C. Neyerlin, R. Mukundan, R.K. Ahluwalia, D.A. Cullen, K.L. More, A.Z. Weber, D.J. Myers, Recent developments in catalyst-related PEM fuel cell durability, Curr. Opin. Electrochem. 21 (2020) 192–200. https://doi.org/10.1016/j.coelec.2020.02.007.

[6] A. Kobayashi, T. Fujii, C. Harada, E. Yasumoto, K. Takeda, K. Kakinuma, M. Uchida, Effect of Pt and Ionomer Distribution on Polymer Electrolyte Fuel Cell Performance and Durability, ACS Appl. Energy Mater. 4 (2021) 2307–2317.

[7] E. Padgett, V. Yarlagadda, M.E. Holtz, M. Ko, B.D.A. Levin, R.S. Kukreja, J.M. Ziegelbauer, R.N. Andrews, J. Ilavsky, A. Kongkanand, Mitigation of PEM fuel cell catalyst degradation with porous carbon supports, J. Electrochem. Soc. 166 (2019) F198.

[8] P.J. Ferreira, Y. Shao-Horn, D. Morgan, R. Makharia, S. Kocha, H.A. Gasteiger, Instability of Pt⁄C electrocatalysts in proton exchange membrane fuel cells: a mechanistic investigation, J. Electrochem. Soc. 152 (2005) A2256.

[9] Y. Shao-Horn, W.C. Sheng, S. Chen, P.J. Ferreira, E.F. Holby, D. Morgan, Instability of supported platinum nanoparticles in low-temperature fuel cells, Top. Catal. 46 (2007) 285–305.

[10] X. Wang, R. Kumar, D.J. Myers, Effect of voltage on platinum dissolution: Relevance to polymer electrolyte fuel cells, Electrochem. Solid State Lett. 9 (2006) A225.

[11] J.P. Braaten, S. Ogawa, V. Yarlagadda, A. Kongkanand, S. Litster, Studying Pt-based fuel cell electrode degradation with nanoscale X-ray computed tomography, J. Power Sources. 478 (2020) 229049.

[12] N. Macauley, L. Ghassemzadeh, C. Lim, M. Watson, J. Kolodziej, M. Lauritzen, S. Holdcroft, E. Kjeang, Pt band formation enhances the stability of fuel cell membranes, ECS Electrochem. Lett. 2 (2013) F33.

[13] S. Chen, H.A. Gasteiger, K. Hayakawa, T. Tada, Y. Shao-Horn, Platinum-alloy cathode catalyst degradation in proton exchange membrane fuel cells: nanometer-scale compositional and morphological changes, J. Electrochem. Soc. 157 (2009) A82.

[14] R.K. Ahluwalia, D.D. Papadias, N.N. Kariuki, J.-K. Peng, X. Wang, Y. Tsai, D.G. Graczyk, D.J. Myers, Potential dependence of Pt and Co dissolution from platinum-cobalt alloy PEFC catalysts using time-resolved measurements, J. Electrochem. Soc. 165 (2018) F3024.

[15] V. Beermann, M.E. Holtz, E. Padgett, J.F. de Araujo, D.A. Muller, P. Strasser, Real-time imaging of activation and degradation of carbon supported octahedral Pt–Ni alloy fuel cell catalysts at the nanoscale using in situ electrochemical liquid cell STEM, Energy Environ. Sci. 12 (2019) 2476–2485.

[16] A.K. Niessen, A.R. Miedema, F.R. De Boer, R. Boom, Enthalpies of formation of liquid and solid binary alloys based on 3d metals: IV. Alloys of cobalt, Phys. B+ C. 151 (1988) 401–432.

[17] N. Ramaswamy, S. Kumaraguru, W. Gu, R.S. Kukreja, K. Yu, D. Groom, P. Ferreira, High-Current Density Durability of Pt/C and PtCo/C Catalysts at Similar Particle Sizes in PEMFCs, J. Electrochem. Soc. 168 (2021) 24519.

[18] J.P. Braaten, X. Xu, Y. Cai, A. Kongkanand, S. Litster, Contaminant Cation Effect on Oxygen Transport through the Ionomers of Polymer Electrolyte Membrane Fuel Cells, J. Electrochem. Soc. 166 (2019) F1337.

[19] D.D. Papadias, R.K. Ahluwalia, N. Kariuki, D. Myers, K.L. More, D.A. Cullen, B.T. Sneed, K.C. Neyerlin, R. Mukundan, R.L. Borup, Durability of Pt-Co alloy polymer electrolyte fuel cell cathode catalysts under accelerated stress tests, J. Electrochem. Soc. 165 (2018) F3166.

[20] K. Shinozaki, Y. Morimoto, B.S. Pivovar, S.S. Kocha, Suppression of oxygen reduction reaction activity on Pt-based electrocatalysts from ionomer incorporation, J. Power Sources. 325 (2016) 745–751.

[21] K. Kodama, A. Shinohara, N. Hasegawa, K. Shinozaki, R. Jinnouchi, T. Suzuki, T. Hatanaka, Y. Morimoto, Catalyst poisoning property of sulfonimide acid ionomer on Pt (111) surface, J. Electrochem. Soc. 161 (2014) F649.

[22] B.T. Sneed, D.A. Cullen, K.S. Reeves, O.E. Dyck, D.A. Langlois, R. Mukundan, R.L. Borup, K.L. More, 3D analysis of fuel cell electrocatalyst degradation on alternate carbon supports, ACS Appl. Mater. Interfaces. 9 (2017) 29839–29848.

[23] T.E. O'Brien, S. Herrera, D.A. Langlois, N.N. Kariuki, H. Yu, M.J. Zachman, D.J.

Myers, D.A. Cullen, R.L. Borup, R. Mukundan, Impact of carbon support structure on the durability of PtCo electrocatalysts, J. Electrochem. Soc. 168 (2021) 54517.

[24] D.R. Baker, D.A. Caulk, K.C. Neyerlin, M.W. Murphy, Measurement of oxygen transport resistance in PEM fuel cells by limiting current methods, J. Electrochem. Soc. 156 (2009).

[25] S. Kabir, D.J. Myers, N. Kariuki, J. Park, G. Wang, A. Baker, N. Macauley, R. Mukundan, K.L. More, K.C. Neyerlin, Elucidating the dynamic nature of fuel cell electrodes as a function of conditioning: an ex situ material characterization and in situ electrochemical diagnostic study, ACS Appl. Mater. Interfaces. 11 (2019) 45016–45030.

[26] T.R. Garrick, T.E. Moylan, V. Yarlagadda, A. Kongkanand, Characterizing electrolyte and platinum interface in PEM fuel cells using CO displacement, J. Electrochem. Soc. 164 (2016) F60.

[27] T. Van Cleve, G. Wang, M. Mooney, C.F. Cetinbas, N. Kariuki, J. Park, A. Farghaly, D. Myers, K.C. Neyerlin, Tailoring electrode microstructure via ink content to enable improved rated power performance for platinum cobalt / high surface area carbon based polymer electrolyte fuel cells, J. Power Sources. 482 (2021) 228889. https://doi.org/10.1016/j.jpowsour.2020.228889.

[28] T. Van Cleve, S. Khandavalli, A. Chowdhury, S. Medina, S. Pylypenko, M. Wang, K.L. More, N. Kariuki, D.J. Myers, A.Z. Weber, S.A. Mauger, M. Ulsh, K.C. Neyerlin, Dictating Pt-Based Electrocatalyst Performance in Polymer Electrolyte Fuel Cells, from Formulation to Application, ACS Appl. Mater. Interfaces. 11 (2019) 46953–46964. https://doi.org/10.1021/acsami.9b17614.

[29] Hydrogen and Fuel Cell Technologies Office Multi-Year Research, Development, and Demonstration Plan, (2014).

[30] H. Yu, M.J. Zachman, K.S. Reeves, J.H. Park, N.N. Kariuki, L. Hu, R. Mukundan, K.C. Neyerlin, D.J. Myers, D.A. Cullen, Tracking Nanoparticle Degradation across

Fuel Cell Electrodes by Automated Analytical Electron Microscopy, ACS Nano. 16 (2022) 12083–12094.

[31] J. Ilavsky, P.R. Jemian, A.J. Allen, F. Zhang, L.E. Levine, G.G. Long, Ultra-small-angle X-ray scattering at the Advanced Photon Source, J. Appl. Crystallogr. 42 (2009) 469–479.

[32] J. Ilavsky, F. Zhang, A.J. Allen, L.E. Levine, P.R. Jemian, G.G. Long, Ultra-small-angle X-ray scattering instrument at the advanced photon source: history, recent development, and current status, Metall. Mater. Trans. A. 44 (2013) 68–76.

[33] J. Ilavsky, Nika: software for two-dimensional data reduction, J. Appl. Crystallogr. 45 (2012) 324–328.

[34] D.J. Myers, A.J. Kropf, E.C. Wegener, H. Mistry, N. Kariuki, J. Park, Degradation of Platinum-Cobalt Alloy PEMFC Cathode Catalysts in Catalyst-Ionomer Inks, J. Electrochem. Soc. 168 (2021) 44510.

[35] B. Ravel, M. Newville, ATHENA, ARTEMIS, HEPHAESTUS: data analysis for X-ray absorption spectroscopy using IFEFFIT, J. Synchrotron Radiat. 12 (2005) 537–541.

[36] B. Patrick, H.C. Ham, Y. Shao-Horn, L.F. Allard, G.S. Hwang, P.J. Ferreira, Atomic structure and composition of “Pt3Co” nanocatalysts in fuel cells: an aberration-corrected STEM HAADF study, Chem. Mater. 25 (2013) 530–535.

[37] K. Shinozaki, H. Yamada, Y. Morimoto, Relative Humidity Dependence of Pt Utilization in Polymer Electrolyte Fuel Cell Electrodes: Effects of Electrode Thickness, Ionomer-to-Carbon Ratio, Ionomer Equivalent Weight, and Carbon Support, J. Electrochem. Soc. 158 (2011) B467. https://doi.org/10.1149/1.3556906.

[38] A. Kongkanand, M.F. Mathias, The priority and challenge of high-power performance of low-platinum proton-exchange membrane fuel cells, J. Phys. Chem. Lett. 7 (2016) 1127–1137.

[39] N. Macauley, D.D. Papadias, J. Fairweather, D. Spernjak, D. Langlois, R. Ahluwalia, K.L. More, R. Mukundan, R.L. Borup, Carbon corrosion in PEM fuel cells and the development of accelerated stress tests, J. Electrochem. Soc. 165 (2018) F3148.

[40] N. Kikkawa, R. Jinnouchi, Does an Ionomer Penetrate a Carbon Mesopore? Free-Energy Analysis Using Molecular Dynamics Simulations, J. Phys. Chem. C. 126 (2022) 11518–11528.

[41] D.K. Paul, K. Karan, Conductivity and wettability changes of ultrathin Nafion films subjected to thermal annealing and liquid water exposure, J. Phys. Chem. C. 118 (2014) 1828–1835.

[42] A. Perego, A. Avid, D.N. Mamania, Y. Chen, P. Atanassov, H. Yildirim, M. Odgaard, I. V Zenyuk, Investigation of cathode catalyst layer interfaces evolution during accelerated stress tests for polymer electrolyte fuel cells, Appl. Catal. B Environ. 301 (2022) 120810.

# Supporting information

# Electrochemical Characterization of Evolving Ionomer/Electrocatalyst Interactions Throughout Accelerated Stress Tests

Leiming Hu[1], Tim Van Cleve[1], Haoran Yu[2], Jae Hyung Park[3], Nancy Kariuki[3], A. Jeremy Kropf[3], Rangachary Mukundan[4ǂ], David A. Cullen[2], Deborah J. Myers[3], KC Neyerlin[1*]

1. Chemistry and Nanoscience Center, National Renewable Energy Laboratory, Golden, CO, USA
2. Center for Nanophase Materials Sciences, Oak Ridge National Laboratory, Oak Ridge, TN, USA
3. Chemical Sciences and Engineering Division, Argonne National Laboratory, Lemont, IL, USA
4. Materials Physics and Applications Division, Los Alamos National Laboratory, Los Alamos, NM, USA

ǂ Current Address: Energy Technologies Area, Lawrence Berkeley National Laboratory, Berkeley, CA 94720

*Corresponding author: Kenneth.Neyerlin@nrel.gov

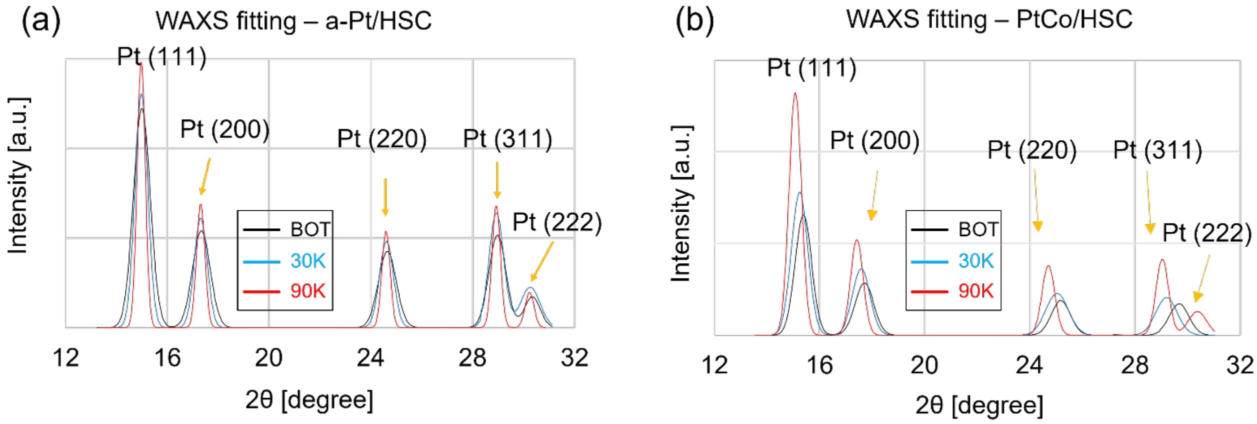

Figure S 1. WAXS peak fitting for (a) a-Pt/HSC and (b) PtCo/HSC.

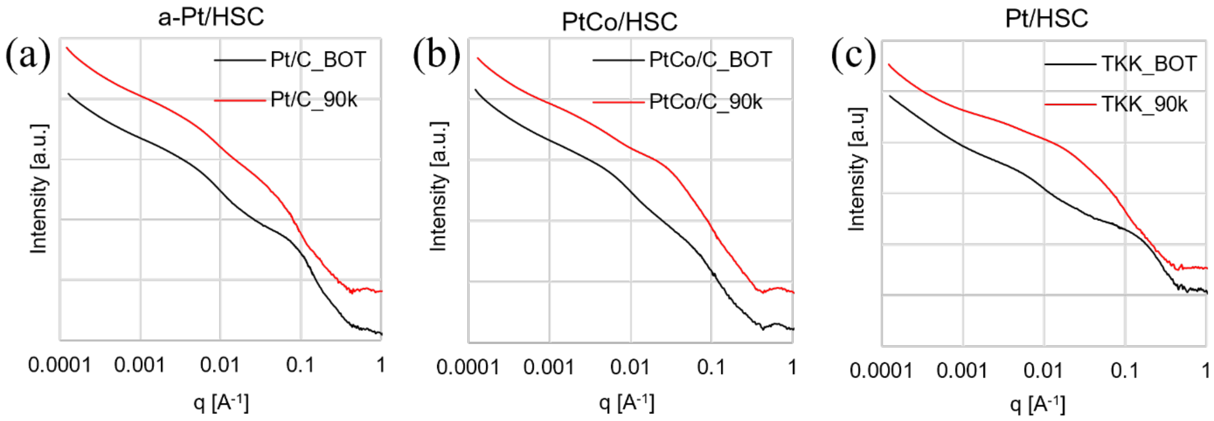

Figure S 2 Ultra-/Small angle X-ray scattering (USAXS/SAXS) profiles for (a) a-Pt/HSC, (b) PtCo/HSC and (c) Pt/HSC before and after application of 90K AST cycles.

Table S1 Mean particle diameter and Co content obtained from SAXS and wide-angle X-ray scattering (WAXS)

|  | a-Pt/HSC mean particle diameter (nm, from SAXS fits) | PtCo/HSC mean particle diameter (nm, from SAXS fits) | PtCo/HSC, Co content (at.%, from WAXS fits) |
|---|---|---|---|
| BOT | 4.6 | 4.7 | 26 |
| 30 K | 4.8 | 5.2 | 15 |
| 90 K | 5.9 | 6.7 | 10 |

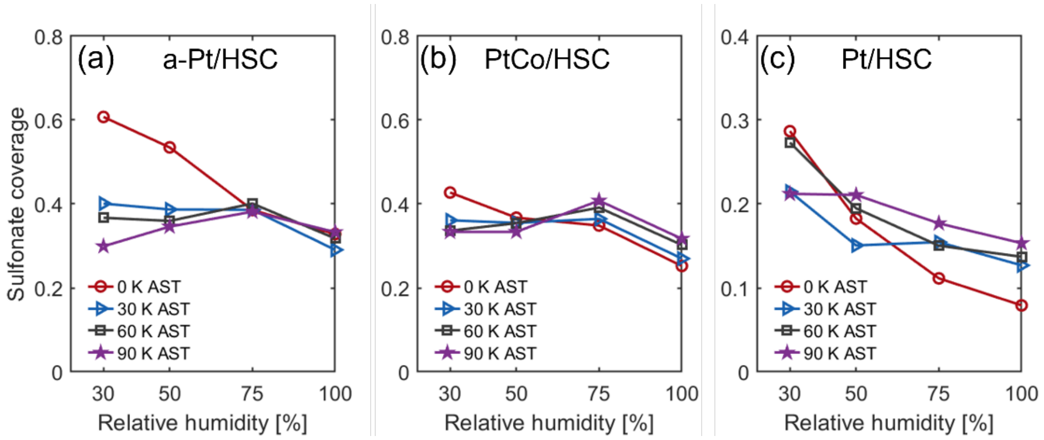

Figure S 3. Sulfonate coverage using CO displacement charge measured at 0.4 V at different RHs (relative to ECA from CO stripping at the same RH). (a) a-Pt/HSC, (b) d-PtCo/HSC and (c) Pt/HSC MEA samples at BOT, after 30 K, 60 K and 90 K AST cycles.

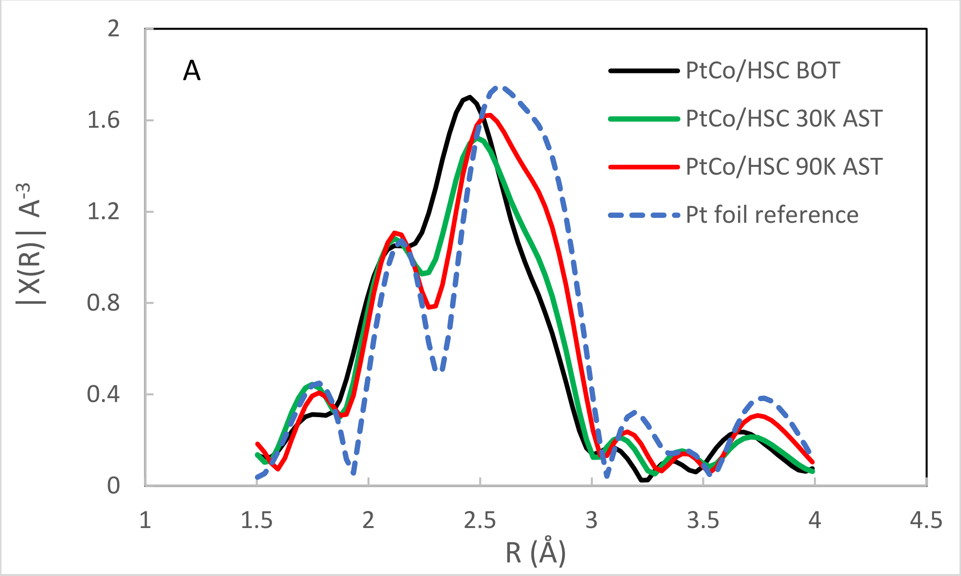

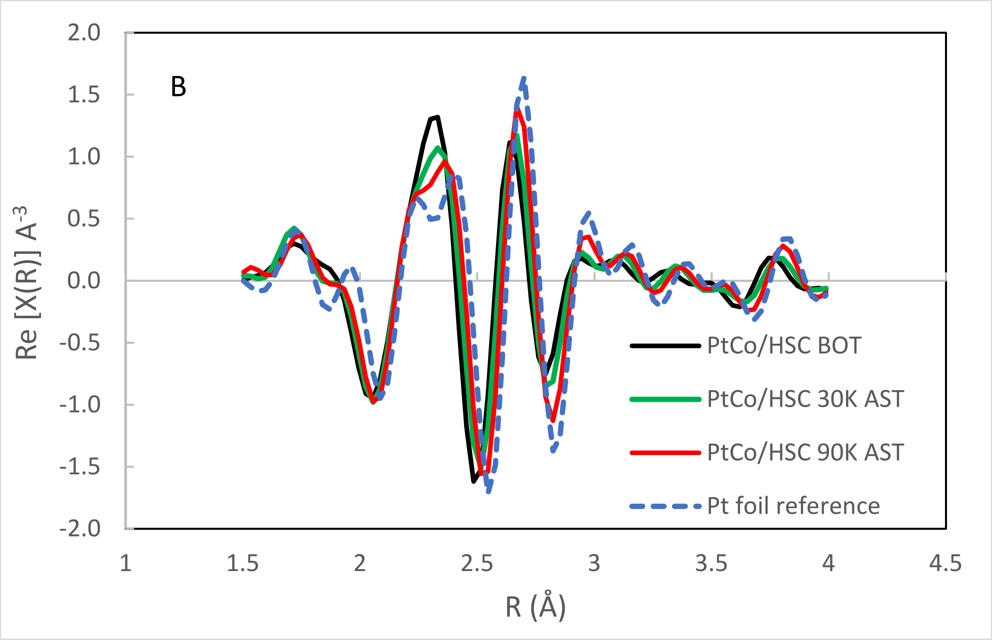

Figure S 4. (A) Magnitude and (B) real part of the Fourier transform of the fine structure of the Pt $L_3$ edge X-ray absorption spectroscopy data of the PtCo/HSC at BOT and after 30K and 90K AST cycles, with Pt foil as the reference.

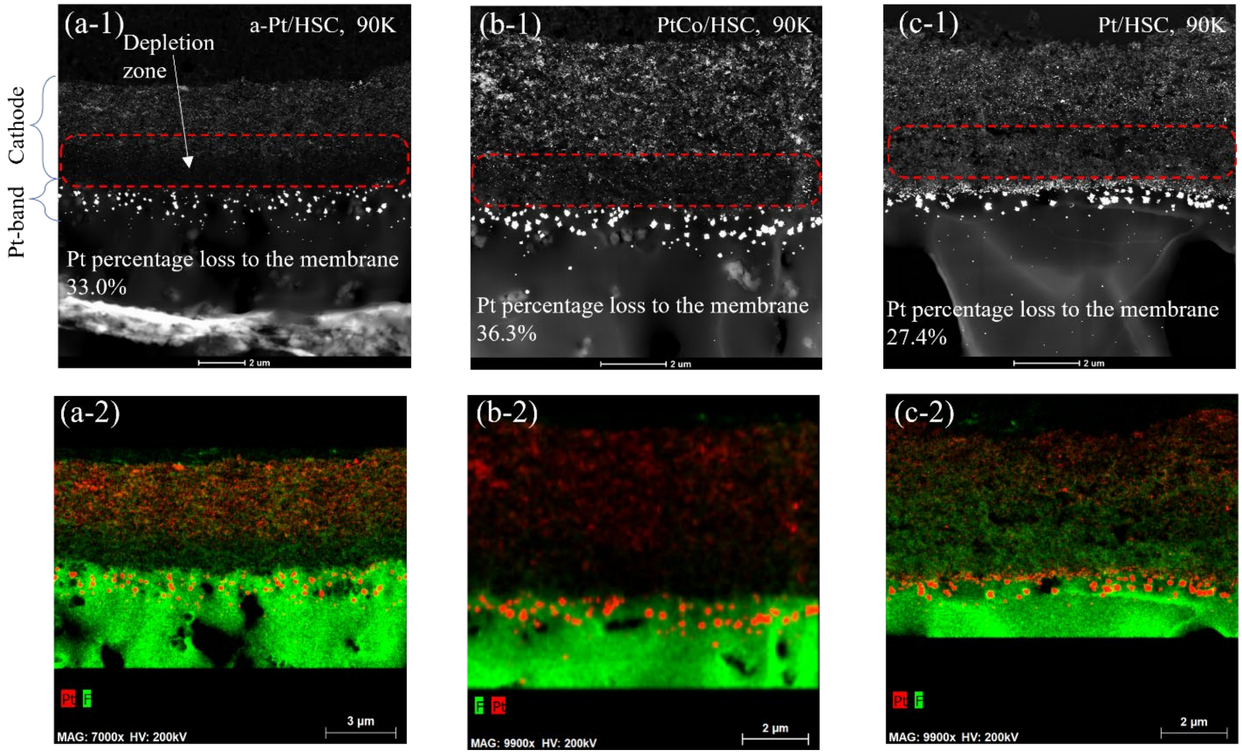

Figure S 5. High-angle annular dark-field (HAADF) images of (a-1) a-Pt/HSC, (b-1) PtCo/HSC (adopted from Yu *et al*. [1] with permission) and (c-1) Pt/HSC after 90K AST cycles, and the corresponding EDS maps (a-2, b-2 and c-2). The corresponding Pt depletion zones in the catalyst layer are marked by the red dashed squares.

## References

[1] H. Yu, M.J. Zachman, K.S. Reeves, J.H. Park, N.N. Kariuki, L. Hu, R. Mukundan, K.C. Neyerlin, D.J. Myers, D.A. Cullen, Tracking Nanoparticle Degradation across Fuel Cell Electrodes by Automated Analytical Electron Microscopy, ACS Nano. 16 (2022) 12083–12094.